Structural Engineering and Mechanics, Vol. 36, No. 1 (2010) 57-78
DOI: http://dx.doi.org/10.12989/sem.2010.36.1.057

A reinforced concrete frame element with shear effect

*Hamid R. Valipour[1] and Stephen J. Foster[2a]

[1]*School of Civil and Environmental Engineering, University of Technology, Sydney, NSW 2007, Australia*
[2]*School of Civil and Environmental Engineering, The University of New South Wales, Sydney, NSW 2052, Australia*

(Received July 20, 2009, Accepted April 30, 2010)

Abstract. A novel flexibility-based 1D element that captures the material nonlinearity and second order *P*-Δ effects within a reinforced concrete frame member is developed. The formulation is developed for 2D planar frames in the modified fiber element framework but can readily be extended to 3D cases. The nonlinear behavior of concrete including cracking and crushing is taken into account through a modified hypo-elastic model. A parabolic and a constant shear stress distribution are used at section level to couple the normal and tangential tractions at material level. The lack of objectivity due to softening of concrete is addressed and objectivity of the response at the material level is attained by using a technique derived from the crack band approach. Finally the efficiency and accuracy of the formulation is compared with experimental results and is demonstrated by some numerical examples.

Keywords: flexibility; framed structures; objectivity; *P*-Δ effects; reinforced concrete; shear.

1. Introduction

In a classical fiber element approach, the Navier-Bernoulli hypothesis is adopted for the distribution of axial strains over the depth of the section and the effect of shear tractions are taken to be negligible. In such a case a uniaxial constitutive law suffices to calculate the stress and stiffness of the fibers and neglecting the shear effect in slender members is reasonable, provided that the member fails in flexure and not in shear. However, for elements with span to depth ratios of less than 5, or the elements subjected to the cyclic loads, the shear effects can dominate the response and must be considered (Petrangeli *et al.* 1999, Sezen 2008). Attempts to take account of the shear effect in the fiber (layer) element follow two specific trends. In the first, shear and axial tractions are coupled at the material level and shear stress field over the section depth are obtained by fulfillment of inter-fiber equilibrium (over the section and along the element) or application of a predefined shear flow (strain) function (Vecchio and Collins 1988, Petrangeli *et al.* 1999). The first approach is more accurate but also more time consuming in comparison with the second.

Over the last two decades, the superior performance of the flexibility and mixed approach in the formulation of frame elements has been demonstrated through different studies (Neuenhofer and Filippou 1997, Taylor *et al.* 2003). The flexibility formulation has been separately used for

*Corresponding author, Senior Lecturer, E-mail: Hamid.Valipour@uts.edu.au
[a]Professor

geometrical and physical nonlinear analysis of frames, however the performance of the materially nonlinear flexibility-based formulations within geometrical nonlinearity has not been investigated thoroughly and it is limited to nonlinear time-dependent analysis of beams and columns.

In this paper a novel flexibility-based frame element based on the total secant stiffness is formulated and the classic fiber element approach is replaced by a numerical integration to improve the formulation efficiency. Recently, similar integration scheme at section level was elaborately used by Shuraim (2001) to devise a variable layering system for nonlinear analysis of reinforced concrete planar frames. Geometrical nonlinearity is taken into account by satisfying the equilibrium equations for the deformed element and a composite Simpson integration scheme, accompanied with a parabolic piecewise interpolation of curvature function is used to establish the deformed shape of the element. In comparison with available methods such as stability functions which already have been used in combination with flexibility formulation (Park and Kim 2008), this novel method of modeling geometrical nonlinearity, offers superior accuracy without any limitation on the element geometry and boundary condition. The effect of shear stress at material level (integration points) is taken into account through a predefined parabolic or constant shear flow. The softening of concrete under tension and compression is taken into account and a crack band concept is employed to restore the objectivity of the results.

2. Flexibility formulation based on the total secant stiffness

In this section, the satisfaction of equilibrium, compatibility and the constitutive laws a direct iteration scheme based on the total secant stiffness approach is established.

2.1 Equilibrium equations

Fig. 1(a) shows a 2-node plane frame element *AB* with three degrees of freedom at each node (2 translations and 1 rotation). The equilibrium of the deformed configuration *Ax* (Fig. 1(b)), yields

$$\mathbf{D}(x) = \mathbf{b}(x)\mathbf{Q}_A + \mathbf{D}^*(x) \tag{1}$$

$$\mathbf{b}(x) = \begin{bmatrix} -1 & 0 & 0 \\ 0 & x & -1 \end{bmatrix} \tag{2}$$

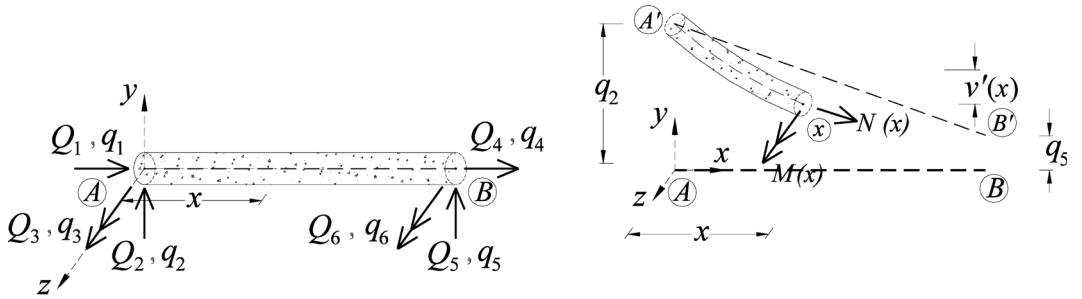

(a) (b)

Fig. 1 (a) 2-node frame element *AB* in *x*-*y* plane, (b) free body diagram of *Ax* with deflection

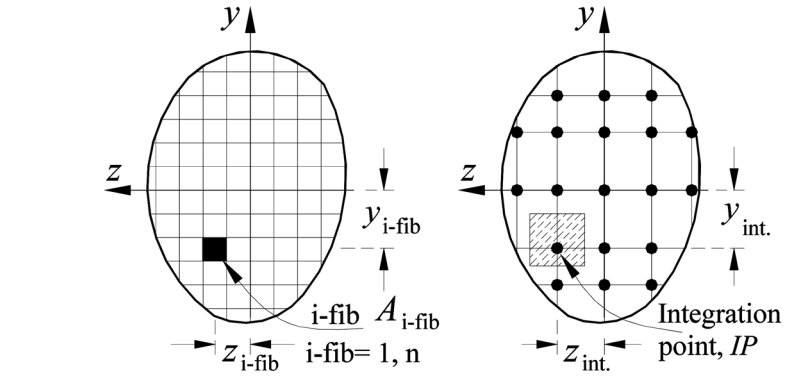

(a)

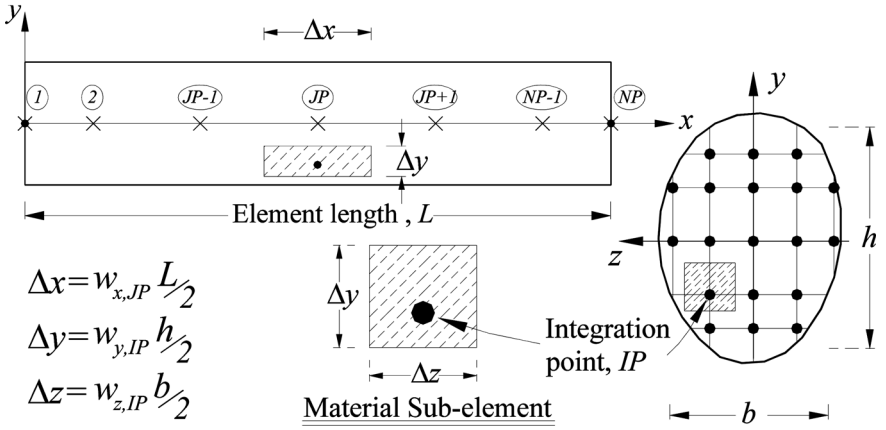

(b)

Fig. 2 (a) Comparison of the classical fiber element and present formulation at section level, (b) side view and cross section of frame element and material sub-element

where, $\mathbf{D}(x) = [N(x) \;\; M(x)]^T$ is a vector of section generalized forces, $\mathbf{b}(x)$ is a force interpolation matrix, $\mathbf{Q}_A = [Q_1 \;\; Q_2 \;\; Q_3]^T$ is a vector of generalized nodal forces at end A and $\mathbf{D}^*(x) = [0 \;\; Q_1 v'(x)]^T$ is vector of undulation effect which represents the deflection of the element with respect to the rotated axis of the element after deformation (Carol and Murcia 1989).

Equilibrium across the section requires that

$$\mathbf{D}(x) = [\int_\Omega \sigma_x dA - \int_\Omega y\sigma_x dA]^T \tag{3}$$

where y is the distance of the integration point from the element mid-plane (see Fig. 2(a)) and σ_x is the first component of the stress vector $\boldsymbol{\sigma} = [\sigma_x \;\; \sigma_y \;\; \tau_{xy}]^T$.

2.2 Compatibility equations and stress-strain relationships

Assuming perfect bond and adopting the Navier-Bernoulli theory, the compatibility requirement is

obtained as

$$\varepsilon_x = \varepsilon_r - y\kappa \tag{4}$$

where ε_x denotes the first component of the strain vector $\boldsymbol{\varepsilon} = [\varepsilon_x \ \varepsilon_y \ \gamma_{xy}]^T$, ε_r denotes the section axial strain and κ is the section curvature. Decomposing the total strain ε_x, to a plastic strain component, ε_{px}, and an elastic strain component, ε_{ex}, the stress at any point in the loading-unloading history of material is given as

$$\sigma_x = E_e(\varepsilon_x - \varepsilon_{px}) \tag{5}$$

where E_e is the elastic total secant modulus of the theoretical unloading/reloading curve with respect to total plastic strain.

If Eqs. (4) and (5) are substituted into Eq. (3), then (Valipour and Foster 2010)

$$\mathbf{D}(x) = {}^e\mathbf{k}_s(x)\mathbf{d}(x) + \mathbf{D}_p(x) \tag{6}$$

$${}^e\mathbf{k}_s(x) = \begin{bmatrix} \int_\Omega E_e dA & -\int_\Omega y E_e dA \\ -\int_\Omega y E_e dA & -\int_\Omega y^2 E_e dA \end{bmatrix} \tag{7}$$

$$\mathbf{D}_p(x) = [-\int_\Omega E_e \cdot \varepsilon_{px} dA \quad \int_\Omega y E_e \cdot \varepsilon_{px} dA]^T \tag{8}$$

where ${}^e\mathbf{k}_s(x)$ is the secant stiffness matrix of the section, $\mathbf{D}_p(x)$ is the residual plastic force vector for the section and $\mathbf{d}(x) = [\varepsilon_r \ \kappa]^T$ is the generalized strain vector of the section. The flexibility matrix of the section, ${}^e\mathbf{f}_s(x)$, is obtained by inverting the section stiffness matrix and then Eq. (6) can be rearranged as

$$\mathbf{d}(x) = {}^e\mathbf{f}_s(x)\{\mathbf{D}(x) - \mathbf{D}_p(x)\} \tag{9}$$

Adopting the small strain assumption within beam theory and applying the principle of virtual work for the cantilever configuration AB clamped at end B and subjected to a virtual load vector $\mathbf{Q}_A$ at end A yields

$$\mathbf{q}_A = \int_0^l \mathbf{b}^T(x)\mathbf{d}(x)dx \tag{10}$$

Substituting Eqs. (1) and (9) into Eq. (10), gives

$$\mathbf{q}_A = {}^e\mathbf{F}_{AA}\mathbf{Q}_A + \mathbf{q}^*_{(A)} - \mathbf{q}_{p(A)} \tag{11}$$

$${}^e\mathbf{F}_{AA} = \int_0^l \mathbf{b}^T(x)\,{}^e\mathbf{f}_s(x)\mathbf{b}(x)dx \tag{12}$$

$$\mathbf{q}_{p(A)} = \int_0^l \mathbf{b}^T(x)\,{}^e\mathbf{f}_s(x)\mathbf{D}_p(x)dx \tag{13}$$

$$\mathbf{q}^*_{(A)} = \int_0^l \mathbf{b}^T(x)\,{}^e\mathbf{f}_s(x)\mathbf{D}^*(x)dx \tag{14}$$

where $\mathbf{q}_A$ is the generalized deformation vector at end A of the element, ${}^e\mathbf{F}_{AA}$ is the flexibility sub-matrix at end A, $\mathbf{q}_{p(A)}$ is a vector of the nodal generalized plastic deformations at end A and $\mathbf{q}^*_{(A)}$ is a vector of nodal generalised deformations due to the undulation effect.

If $\mathbf{Q}_{p(A)} = {}^e\mathbf{K}_{AA}\mathbf{q}_{p(A)}$ and $\mathbf{Q}^*_{(A)} = {}^e\mathbf{K}_{AA}\mathbf{q}^*_{(A)}$ represent the generalised force vectors corresponding with deformation vectors $\mathbf{q}_{p(A)}$ and $\mathbf{q}^*_{(A)}$, respectively, Eq. (11) degenerates to

$$ {}^e\mathbf{K}_{AA}\mathbf{q}_A = \mathbf{Q}_A + \mathbf{Q}^*_{(A)} - \mathbf{Q}_{p(A)} \tag{15}$$

where ${}^e\mathbf{K}_{AA}$ is the stiffness sub-matrix at end A and is obtained by inverting ${}^e\mathbf{F}_{AA}$.

Solving the equilibrium equations for the cantilever frame element clamped at end A and subjected to nodal forces at end B yields similar equations that assembles to the element secant stiffness matrix ${}^e\mathbf{K}_e$

$$ {}^e\mathbf{K}_e = \begin{bmatrix} [{}^e\mathbf{F}_{AA}]^{-1} & [{}^e\mathbf{F}_{AA}]^{-1}\Gamma \\ \Gamma^T[{}^e\mathbf{F}_{AA}]^{-1} & \Gamma^T[{}^e\mathbf{F}_{AA}]^{-1}\Gamma \end{bmatrix} \tag{16}$$

$$ \mathbf{Q}_p = \begin{bmatrix} \mathbf{Q}_{p(A)} \\ \Gamma^T\mathbf{Q}_{p(A)} \end{bmatrix} \tag{17}$$

$$ \mathbf{Q}^* = \begin{bmatrix} \mathbf{Q}^*_{(A)} \\ \Gamma^T\mathbf{Q}^*_{(A)} \end{bmatrix} \tag{18}$$

where $\mathbf{Q}_p$ is the element nodal plastic force vector, $\mathbf{Q}^*$ is the element nodal force vector due to undulation effect and Γ is the transformation matrix defined as

$$ \Gamma = \begin{bmatrix} -1 & 0 & 0 \\ 0 & -1 & L \\ 0 & 0 & -1 \end{bmatrix} \tag{19}$$

Using Eqs. (15) to (18) and satisfying the equilibrium equations for the deformed element $A'B'$ (see Fig. 1(b)) leads to element matrix formulation as

$$ {}^e\mathbf{K}_e\mathbf{q} = \mathbf{Q} + \mathbf{Q}^* - \mathbf{Q}_p - \mathbf{Q}_{P-\Delta} \tag{20}$$

$$ \mathbf{Q}_{P-\Delta} = [0 \;\; Q_1(q_5 - q_2)/l \;\; 0 \;\; 0 \;\; Q_1(q_2 - q_5)/l \;\; 0]^T \tag{21}$$

where $\mathbf{Q}_{P-\Delta}$ is a vector of generalised nodal forces due to P-Δ effect.

In this study all of the integrals appearing in the formulation are calculated numerically. For this purpose a network of integration points is required to be provided along the element axis and over the section depth (Fig. 2(a)). In providing a network of integration points the element domain is divided into small imaginary sub-elements with dimensions (i.e., Δx, Δy and Δz) that are proportional to the element (section) size and the integration point weight factor, w_{IP}, (see Fig. 2(b)).

3. Displacement interpolation along the element

In the displacement-based formulation the deformed shape of the element can be obtained by nodal displacement values and adopted shape functions. In the force-based element, however, there is no displacement shape function to be used and a different technique such as curvature-based displacement interpolation is required (Neuenhofer and Filippou 1998).

Adopting the small strains and slope within the Navier-Bernoulli beam theory leads to the following strain-displacement relationships for an arbitrary section at x along the element (Fig. 3)

$$v(x) = q_2 + xq_3 + \int_0^x (x-s)\kappa(s)ds \tag{22}$$

where $v(x)$ is the lateral displacement of the section at x. With regards to Fig. 3, the undulation deflection $v'(x)$ is calculated as follows

$$v'(x) = \left\{\frac{(q_5-q_2)}{l} - q_3\right\}x - \int_0^x (x-s)\kappa(s)ds \tag{23}$$

In this study a composite Simpson integration method is employed to estimate the integrals along the element axis, which is more straightforward and less costly compared with existing methods. Using the composite Simpson scheme, the integral on the right side of the Eq. (23) can be estimated easily for the odd numbered longitudinal sections. For the even numbered sections a piecewise parabolic interpolation of curvature function is used. A composite Simpson scheme with $(2n+1)$ integration point along the element axis divides the element to n equal sub-elements. It is assumed that the curvature varies parabolic along each sub-element (Fig. 3). Having the value of curvatures for mid and end nodes of the sub-element, a 2nd order parabola is used to interpolate the curvature along the sub-element and using this 2nd order parabola the integral in Eq. (23) can be calculated analytically for the even numbered sections.

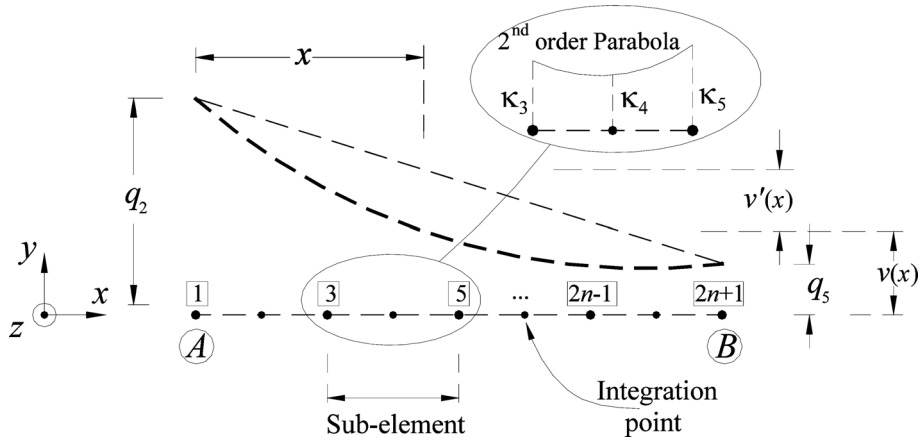

Fig. 3 Outline of the composite Simpson integration scheme, element and sub-elements

4. Material constitutive laws

Regardless of the simplifications made for formulating reinforced concrete beam elements, the response of the element depends strongly on concrete constitutive law. Application of computationally expensive concrete models within reinforced concrete beam elements reduces the efficiency and simplicity of the analysis that are the appealing features of the 1D element. In this study a nonlinear orthotropic model based on the equivalent uniaxial strain concept is recast in the framework of the total strain (secant) formulation and consistent with damage models. The early models of this kind were limited to 2D cases and proportional monotonic loading (Darwin and Pecknold 1974), whereas the newer versions are able to model the concrete behavior under cyclic loadings and take account of confining effects in 3D cases (Balan *et al.* 2001, He *et al.* 2006). More recently, the concepts of total strain, orthotropic models and modified compression field theory have been combined to develop a hysteretic material model for planar reinforced concrete elements (Yun *et al.* 2008).

The stress-strain relationship for an orthotropic material in total secant formulation takes the form

$$\mathbf{s} = \mathbf{D}_{\text{sec}}\mathbf{e} \tag{24}$$

where, $\mathbf{s} = [\sigma_1 \ \sigma_2 \ \tau_{12}]^T$ and $\mathbf{e} = [\varepsilon_1 \ \varepsilon_2 \ \gamma_{12}]^T$ represent the total stress and strain vector, respectively. Subscripts 1 and 2 denote the current axes of orthotropy and $\mathbf{D}_{\text{sec}}$ is the total secant stiffness matrix of the material in the local 1-2 coordinate system. The expansion of the recent stress-strain relationship in 1-2 coordinate systems may be approximated in the symmetric form as (Darwin and Pecknold 1974)

$$\mathbf{D}_{\text{sec}} = \frac{1}{1-\upsilon^2}\begin{bmatrix} E_1 & \upsilon\sqrt{E_1E_2} & 0 \\ \upsilon\sqrt{E_1E_2} & E_2 & 0 \\ 0 & 0 & (1-\upsilon^2)G^* \end{bmatrix} \tag{25}$$

where υ is the Poisson ratio, G^* is a crack modified shear modulus and E_1 and E_2 are secant moduli of elasticity corresponding with directions 1 and 2, respectively.

The Poisson ratio is taken as $\upsilon = \upsilon_0 = 0.2$, for the compression-compression state and for the other states it is reduced by

$$\upsilon = \begin{cases} \upsilon_0(1-\varepsilon_{1(2),eq}/\varepsilon_{ut}) & \varepsilon_t \le \varepsilon_{1(2)} \le \varepsilon_{ut} \\ 0 & \varepsilon_{ut} \le \varepsilon_{1(2)} \end{cases} \tag{26}$$

where $\varepsilon_{1(2),eq}$ represents the equivalent tensile strain in direction 1(2).

The shear modulus follows two different paths, depending on the cracking state in the concrete. For the case of uncracked concrete, the shear modulus remains invariant by adopting (Darwin and Pecknold 1974)

$$(1-\upsilon^2)G^* = 0.25(E_1 + E_2 - 2\upsilon\sqrt{E_1E_2}) \tag{27}$$

For cracked concrete, the invariance of the constitutive law is maintained by adopting (Crisfield and Wills 1989)

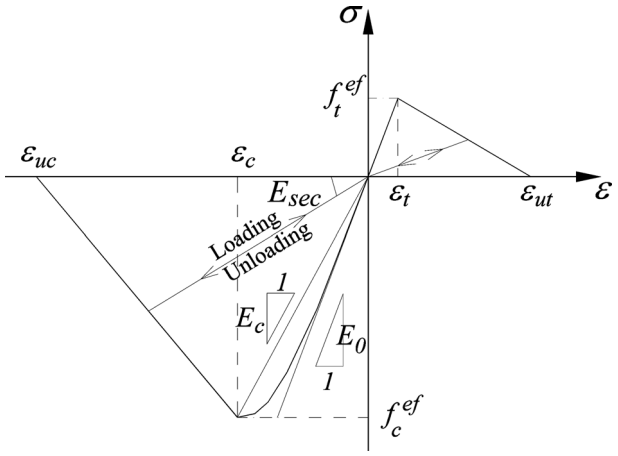

Fig. 4 Equivalent uniaxial stress-strain law for concrete under tension and compression

$$G^* = \frac{(\sigma_u - \sigma_v)}{2(\varepsilon_u - \varepsilon_v)} \tag{28}$$

where $\sigma_{u(v)}$ and $\varepsilon_{u(v)}$ represent the principal stresses and strains, respectively.

The equivalent uniaxial stress-strain diagram is shown in Fig. 4 (tensile strains taken as positive) and the equivalent uniaxial strain (in the i direction) $\varepsilon_{i,eq}$, is calculated from

$$\varepsilon_{i,eq} = \frac{1}{1-\upsilon^2}\left(\varepsilon_i + \upsilon\sqrt{\frac{E_j}{E_i}}\varepsilon_j\right), \quad (i \neq j)i,j = 1,2 \tag{29}$$

The CEB-FIP model code 1990 stress-strain relationship is adopted for the ascending branch of the concrete under compression with a linear descending branch. For concrete in tension, a linear elastic law is employed. The unloading/reloading follows the total secant line to the origin (see Fig. 4). The effective compressive and tensile strength of concrete are denoted as f_c^{ef} and f_t^{ef}, respectively, ε_c and ε_t denote the strain corresponding with effective compressive and tensile strength, respectively, ε_{uc} and ε_{ut} represent the compressive and tensile strains, respectively, that correspond to the second point of zero stress and are adjusted with respect to the crack band model and the adopted integration scheme. The confining effect on the concrete ductility and strength can be modeled by modifying the compressive strength, f_{cc}^{ef}, the corresponding strain, ε_{cc}, and the compressive ultimate strain, ε_{ucc}, according to available uniaxial models (Mander *et al.* 1988).

The effective strength of the material and their corresponding strain is obtained from the bi-axial failure envelope of the concrete (see Fig. 5). In the compression-compression region the effective compressive strength (in direction 2) is obtained according to Kupfer *et al.* (1969) failure criterion as

$$f_{2c}^{ef} = \frac{1 + 3.65\alpha}{(1+\alpha)^2} f_c, \quad \alpha = \frac{\sigma_1}{\sigma_2} \leq 1.0 \tag{30}$$

where f_c is the uniaxial compressive strength of concrete. In the tension-tension zone, the effective tensile strength is equal to the concrete uniaxial tensile strength, f_t. That is $f_{1t}^{ef} = f_{2t}^{ef} = f_t$.

The tension-compression stress state consists of two parts. For $\alpha \leq -0.2$ the effective tensile

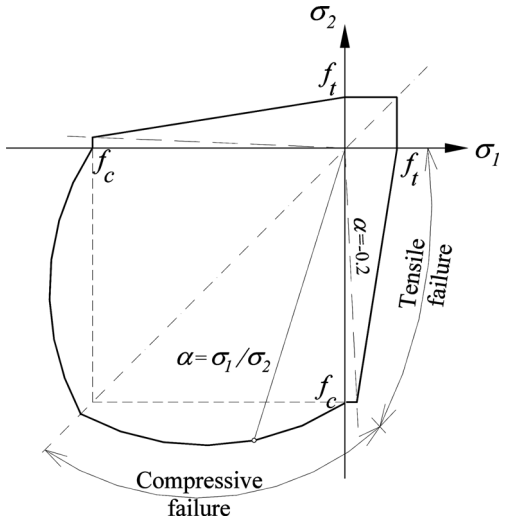

Fig. 5 Schematic bi-axial failure curve of concrete in stress space

strength is reduced according to

$$f_{1t}^{ef} = (1 + 0.8\sigma_2/f_c)f_t, \quad \sigma_2 \le 0 \le \sigma_1 \tag{31}$$

For the case of $-0.2 \le \alpha \le 0$, the concrete cracks in the 1-direction simultaneously with the onset of crushing in the 2-direction.

5. Solution scheme at material level

In this study a direct total secant iterative scheme is used to capture the post-peak response of the concrete. At each section of a beam element two different groups of imaginary material sub-elements are adopted to obtain the material response. The first are out-of-core sub-elements and the second are in-core sub-elements (Fig. 6(a)).

A typical in-core sub-element of depth Δy and length Δx is decomposed to the concrete and transverse reinforcement components, as shown in Fig. 6(b). The response of the sub-element can be obtained by superimposing the concrete and reinforcement responses through equilibrium, compatibility and fulfillment of the constitutive laws. The assumptions of smeared transverse reinforcements and perfect bond are adopted within the sub-element formulation.

The value of the strain ε_x and shear stress τ_{xy} at each sub-element is available from compatibility and from the prescribed shear stress distribution, respectively. Furthermore the total normal stress acting on the sub-element in the y-y direction (see Fig. 6(b)) is assumed to be negligible (i.e., $\sigma_{ty} = 0$); however, this term is not dropped in the governing equations. Because this recent assumption is a simplification made in existing formulations of this kind and later in this paper a method based on the equilibrium of two adjacent sections is presented to calculate σ_{ty}. With the values of ε_x, τ_{xy} and σ_{ty} available, the iterative algorithm for material state determination at sub-element level is summarized as follows:

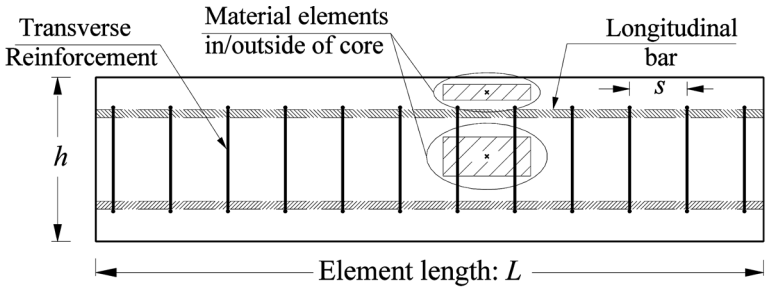

(a)

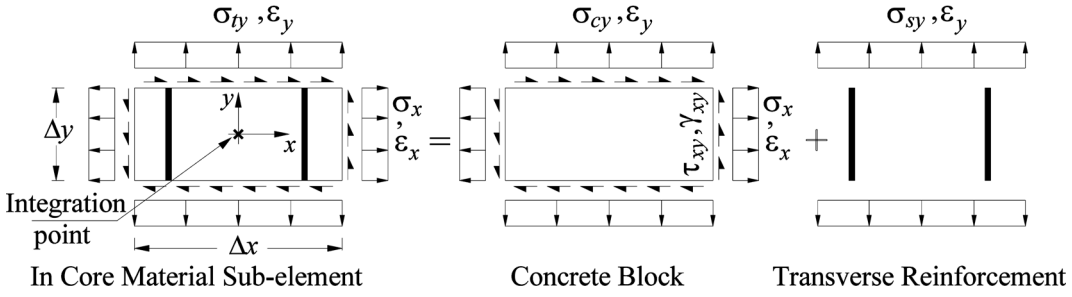

(b)

Fig. 6 (a) Side view of the beam and material sub-elements inside and outside of the core, (b) decomposition of a typical in core sub-element to concrete and steel components

Step (1): The secant stiffness matrix of the concrete block, ${}^{i}\mathbf{C}_{\text{sec}}$, in global x-y coordinate system is established (left superscript i denotes the iteration number)

$$ {}^{i}\mathbf{C}_{\text{sec}} = \mathbf{T}_{\varepsilon}^{Ti}\mathbf{D}_{\text{sec}}\mathbf{T}_{\varepsilon} \tag{32} $$

where $\mathbf{T}_{\varepsilon}$ is the strain transformation matrix. The stiffness matrix, $\mathbf{C}_{\text{sec}}$, relates the stress vector of the concrete block (Fig. 6(b)) $\boldsymbol{\sigma}_c = [\sigma_x \ \sigma_{cy} \ \tau_{xy}]^T$ to strain vector $\boldsymbol{\varepsilon}_c = \boldsymbol{\varepsilon} = [\varepsilon_x \ \varepsilon_{cy} \ \gamma_{xy}]^T$; that is $\boldsymbol{\sigma}_c = \mathbf{C}_{\text{sec}}\boldsymbol{\varepsilon}_c$. For computational efficiency, the terms of $\mathbf{C}_{\text{sec}}$ (i.e., c_{11}, c_{12} c_{33}) for Eq. (32) should be pre-multiplied (refer Appendix).

Step (2): The following set of equations is solved and the vector of unknowns ${}^{i}\mathbf{u} = [\sigma_x \ \ \varepsilon_y \ \ \gamma_{xy}]^T$ is obtained

$$ \sigma_{cy} = \sigma_{ty} - \rho_s\sigma_{sy}, \quad \rho_s = \frac{A_s'}{bs} \tag{33} $$

$$ \begin{bmatrix} 1/c_{11} & -c_{12}/c_{11} & -c_{13}/c_{11} \\ c_{12}/c_{11} & (c_{22}-c_{12}^2/c_{11}) & (c_{23}-c_{12}c_{13}/c_{11}) \\ c_{13}/c_{11} & (c_{23}-c_{12}c_{13}/c_{11}) & (c_{33}-c_{13}^2/c_{11}) \end{bmatrix} \begin{bmatrix} \sigma_x \\ \varepsilon_y \\ \gamma_{xy} \end{bmatrix} = \begin{bmatrix} \varepsilon_x \\ \sigma_{cy} \\ \tau_{xy} \end{bmatrix} \tag{34} $$

where A'_s, s and ρ_s are area, step and ratio of transverse reinforcement, respectively, and b is the section width. According to the author's experience during this step doing a few iterations to calculate σ_{sy} corresponding with ε_y, improves the overall efficiency of the algorithm. In such a case, the initial value of σ_{sy} is used to calculate the σ_{cy} from Eq. (33). The current value of σ_{cy} is substituted in Eq. (34) for calculating the vector of unknowns, ${}^{i}\mathbf{u}$. The new value of ε_y is used to correct the σ_{sy} and inner iteration loop goes back to Eq. (33) for calculating the updated σ_{cy}. This loop is repeated until the convergence criterion is satisfied.

Step (3): With ${}^{i}\boldsymbol{\sigma}_c$ and ${}^{i}\boldsymbol{\varepsilon}_c$ on hand, the orientation of the principal stress (strain) coordinate and the value of principal stresses (strains) are updated.

Step (4): The updated value of principal stresses (${}^{i+1}\sigma_1$, ${}^{i+1}\sigma_2$) are used to determine the effective strength of the material and their corresponding strains.

Step (5): The updated values of the principal strains (${}^{i+1}\varepsilon_1$, ${}^{i+1}\varepsilon_2$) are calculated and then the equivalent uniaxial strains are determined from Eqs. (26) and (29).

Step (6): The new stresses and secant modulus in the principal directions (${}^{i+1}E_1$, ${}^{i+1}E_2$) are obtained based on the adopted equivalent uniaxial stress-strain relationship (Fig. 4) and the current values of the equivalent uniaxial strains (${}^{i+1}\varepsilon_{1,eq}$, ${}^{i+1}\varepsilon_{2,eq}$).

Step (7): The convergence criterion at the material level is checked and, if satisfied, then the material state procedure is completed and the solution is continued for the other material sub-elements. Otherwise, the iteration is continued by returning to step (1).

The above explained material state determination algorithm is incorporated within a direct total secant solution strategy at element (structure) level (Valipour and Foster 2010).

6. Treatment of shear

Coupling the shear and normal tractions at material level in a 1D frame element can be carried out by two different methods; iterative fulfillment of inter-fiber equilibrium (over the depth of two adjacent sections) or application of a predefined function for shear flow (strain). The first approach is more accurate but time consuming while the second is more robust and efficient but is less accurate. Furthermore, according to Vecchio and Collins (1988) application of a predefined shear

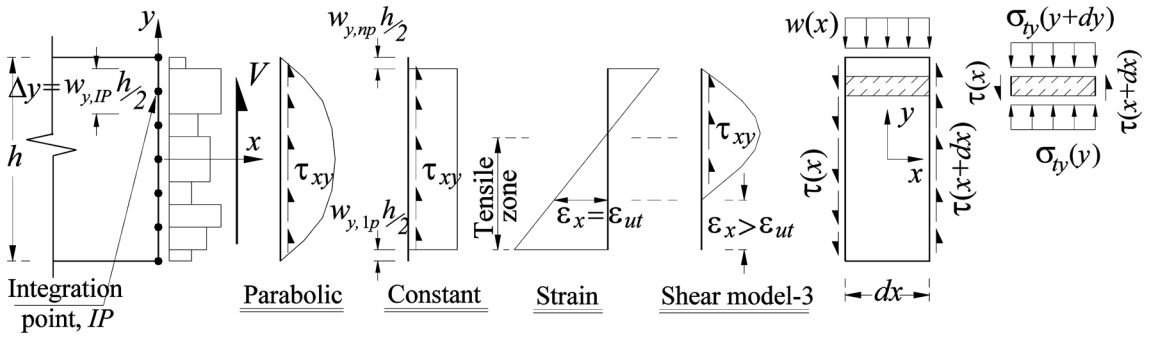

Fig. 7 (a) Section side view and integration points along with parabolic and constant shear stress distribution, (b) relation between axial strain and shear model-3, (c) differential segment subjected to shear and normal stresses

strain underestimates the strains (displacements) whereas a kinetic shear constraint (i.e., predefined shear flow) underestimates the ultimate strength. In this study two different types of kinetic shear constraint (i.e., parabolic and constant shear flow) are used and their performance is examined (Fig. 7(a)). The parabolic and constant shear stress distribution over the depth h of a rectangular section with width b is

$$\tau_{xy} = \frac{3V}{2bh} = \left\{1 - \left(\frac{2y}{h}\right)^2\right\} \tag{35}$$

$$\tau_{xy} = \frac{V}{b(h - h_0)}, \quad h_0 = (w_{y,1p} + w_{y,np})\frac{h}{2} \tag{36}$$

where V is the total shear force acting on the section and $w_{y,1p}$ and $w_{y,np}$ represent the weight factor of the first and the last transverse integration points on the top and bottom chords of the section (Fig. 7(a)), respectively. These hypothetical kinetic constraints usually lead to overestimation of the shear carried by the tensile zone. However, the mechanisms of the aggregate interlock and dowel action that is not captured by these models partially compensate this weakness.

While imposing a predefined shear flow over the total depth of section improves the accuracy of the element, it cannot properly model the shear failure of the sections caused by diagonal cracking of the member or by crushing in the compressive zone of the section. A remedial method for treating this weakness is to impose the shear just over compressive zone and that part of the tensile zone where crack bridging exists. With regards to the concrete model adopted in this study, if the tensile strain at a fiber (integration point) is larger than ε_{ut} the governing equations at the material level are unsolvable as the material has already cracked and the point cannot carry any shear traction. In this case the shear flow is imposed on the part of the section with a strain of less than ε_{ut} (Fig. 7(b)). Shear failure is determined if the governing set of equations for all of the integration points over the aforementioned zones can not be solved. In other words at the incident of the shear failure the material points that carry the shear stresses are completely damaged due to diagonal cracking (or crushing) based on the 2D hypo-elastic model. This model is called shear model-3 in the numerical examples that follow.

Having the shear stress distribution assigned, the normal stress field, σ_{ty}, can be calculated by satisfying the differential equation of equilibrium (Fig. 7(c))

$$\frac{d\tau_{xy}}{dx} + \frac{d\sigma_{ty}}{dy} = 0 \tag{37}$$

Substituting the predefined shear stress distribution in Eq. (37) and then integrating the resulting relationship with respect to y, gives an explicit function for σ_{ty}. For example, using a parabolic shear distribution, leads to

$$\sigma_{ty} = \frac{w(x)}{b}\left\{\frac{1}{2} + \frac{3}{2}\left(\frac{y}{h}\right) - 2\left(\frac{y}{h}\right)^3\right\} \tag{38}$$

where $w(x)$ is the distributed load imposed on the top chord of the frame element. Eq. (38) implies that the stress field σ_{ty} is zero for elements without any distributed load. In reality, however, due to non-uniform shear stress gradient along the element axis σ_{ty} is not zero.

7. Localization limiters and mesh objectivity

Since the softening response of concrete is considered in this study, the problems of objectivity and spurious mesh sensitivity (i.e., mesh size effect and orientation bias) need to be addressed. In rate independent models, the objectivity of results can be restored by introducing a characteristic length into the material model. This characteristic length is introduced in the framework of the crack band (cohesive crack) approach or nonlocal models (Bazant and Oh 1983, Bazant and Jirasek 2002, de Borst 2003).

In frame elements the softening of response and lack of objectivity happens at two levels; at material points due to cracking of tensile concrete or crushing of compressive concrete, and at element level due to crushing of concrete over a plastic hinge zone. In this research a simple method based on the crack band concept is employed to attain the objectivity at material level. A similar technique in the framework of the microplane model has been successfully used in the FEM context (Cervenka *et al.* 2005).

In previous sections it was noted that the provided network of integration points divides the element domain to small sub-elements. In analogy with displacement-based elements in the FEM context, these sub-elements are similar to low order constant stress-constant strain elements that work with crack band (fictitious crack) models properly (Cervenka *et al.* 1995). Fig. 8(a) shows one of these sub-elements in the softening state. According to crack band approach, in this sub-element the localization zone softens (corresponding with point B in Fig. 8(b)), whereas the remaining part of the element unloads through the branch AO (see Fig. 8(b)). The compatibility of the displacement in 1-1 direction, yields

$$l\varepsilon = h\varepsilon_b + (l-h)\varepsilon_u \tag{39}$$

where ε is the sub-element strain in the 1-1 direction which is the principal stress (strain) axis according to the concrete model used in this study, h denotes the crack band width (3 to 5 times of the maximum aggregate), ε_b denotes the uniform softening strain over the band width and ε_u denotes the strain in the unloading zone of the sub-element. With regards to Fig. 8(b) and

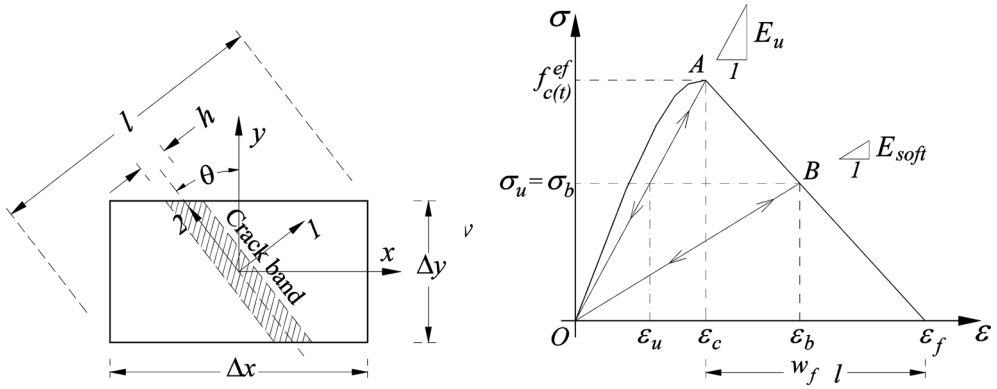

(a) (b)

Fig. 8 (a) Typical softened sub-element, (b) correspondence of stresses and strains for the softened sub-element

equilibrium in the 1-1 direction, Eq. (39) leads to

$$\frac{1}{E_{elem-1}} = \frac{(h/l)}{E_{soft}} + \frac{(1-h/l)}{E_u}, \quad h \le l \tag{40}$$

where, $E_{elem\text{-}1}$ is the sub-element secant modulus in direction 1-1, E_{soft} is the softening secant modulus, E_u is the unloading secant modulus from the peak stress and l is the equivalent length of element in the 1-1 direction, which is obtained based on sub-element size and the rotation of principal coordinate θ. If within step (6) of the solution procedure the current equivalent tensile strain in the principal direction j-j ($j = 1, 2$) lies in the softening regime, the value of $E_{elem\text{-}j}$ is calculated from Eq. (40) and it is used in place of the secant modulus in the following steps of the solution algorithm. The method proposed preserves the original stress-strain relationship for the softening branch, whereas the original crack band model alters this relationship. This advantage resolves the snap back problem associated with large size sub-elements that occur in the original crack band approach.

The objectivity of results for compressive softening is restored by a fictitious crushing plane model and adjusting the ultimate compressive strain, ε_f. In this model compressive displacements and energy dissipation are localized in a crushing plane normal to the direction of compressive principal stress and the value of displacement w_f is independent of the structure size. The value of w_f varies from 0.4 mm to 0.7 mm for normal weight concrete and it is less than 0.3 mm for light weight aggregate concrete (Markeset and Hillerborg 1995). Having the element equivalent length l from the sub-element geometry (Fig. 8(a)), the adjusted value of ultimate strain ε_f is calculated (Fig. 8(b)),

$$\varepsilon_f = \varepsilon_c + \frac{w_f}{l} \tag{41}$$

8. Numerical examples

8.1 Burns and Siess beam

In this example, the simply supported beam of Burns and Siess (1962) subjected to a point load at mid span is analyzed (Fig. 9). The material properties for the specimen are $f_y = 315$ MPa, $E_s = 2.03 \times 10^5$ MPa, $f_t = 2.3$ MPa, $E_c = 2.6 \times 10^4$ MPa, $f_c = 33$ MPa, $\varepsilon_c = 0.002$, $\varepsilon_{uc} = 0.006$,

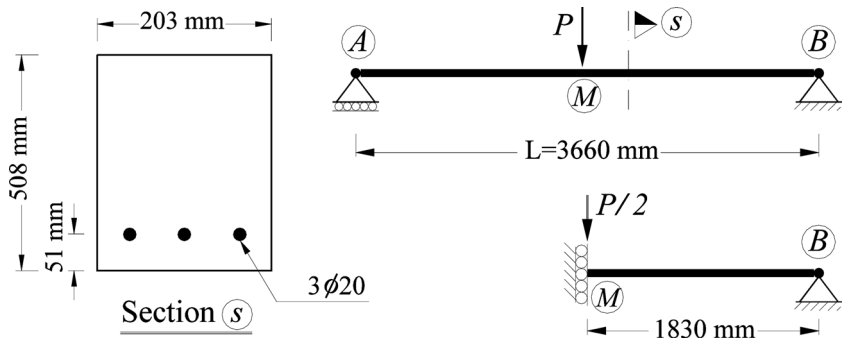

Fig. 9 Geometry of the simple beam, cross section details and idealised FE model

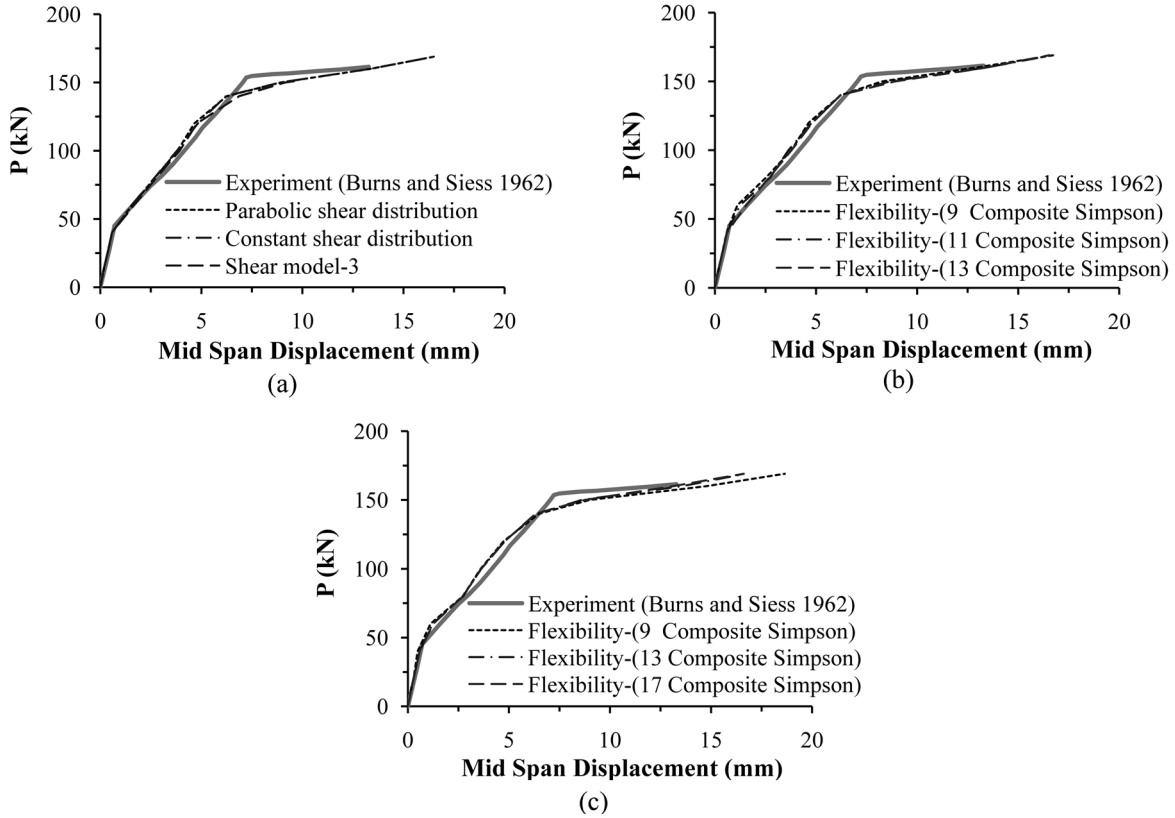

Fig. 10 Load versus mid span displacement response of Burns and Siess beam within different, (a) types of shear distribution, (b) numbers of integration points along the element, (c) numbers of integration points through the section depth

w_f = 0.5 mm and the crack band width is 50 mm.

One half of the beam was modeled by a single flexibility-based element (Fig. 9). The load versus mid-span displacement of the beam is shown in Fig. 10(a). The value of failure load obtained from experiment, constant shear, parabolic shear and shear model-3 are 161 kN, 170 kN, 170 kN and 153 kN, respectively. It is observed that the shear model-3 underestimate the failure load, whereas the constant and parabolic shear distributions overestimates the failure load.

Fig. 10(b) shows the results of analyses undertaken for 15 composite Simpson's integration points through the depth and varying number of points along the length. In Fig. 10(c) the number of points along the length was kept constant (11 points) with the number of points through the depth varied. The figures show that, providing a sufficiently fine mesh is adopted in each direction, the results obtained are independent of the mesh grading. Further, the cracking load predicted by the formulation is fairly accurate.

8.2 Bresler and Scordelis beam

Beam 0A-3 (Fig. 11) tested by Bresler and Scordelis (1963) was analyzed to show the capability of the formulation for predicting shear failure (the beam has no shear reinforcement). The material

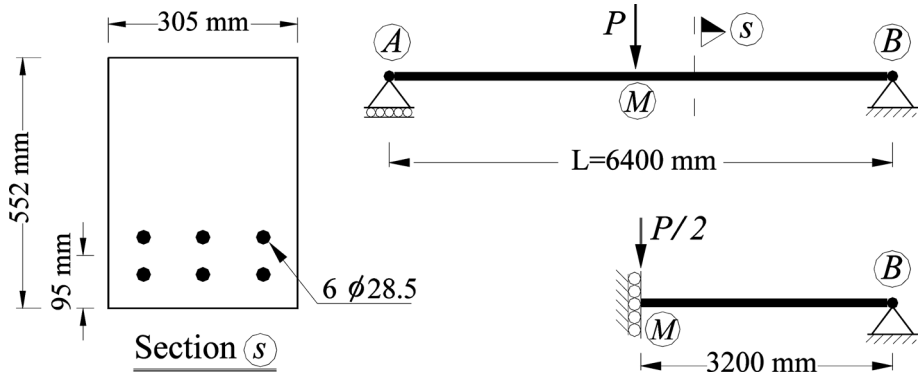

Fig. 11 Geometry of beam and details of section

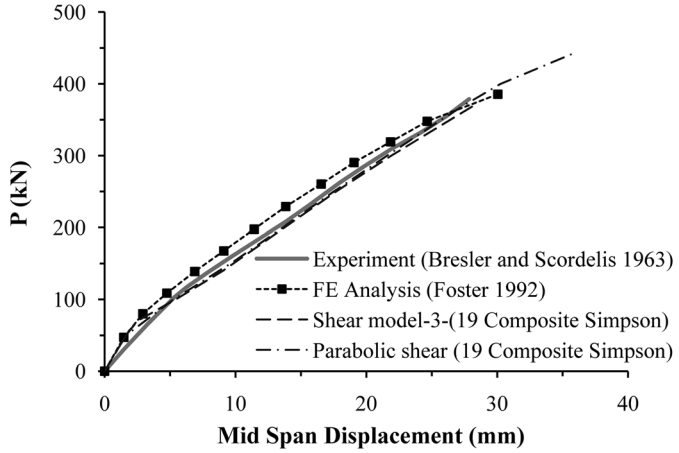

Fig. 12 Load versus mid-span displacement

properties are f_y= 550 MPa, E_s= 2.06 × 10^5 MPa, f_t= 2.4 MPa, E_c= 3.6 × 10^4 MPa, f_c = 36.6 MPa, ε_c = 0.002, ε_{uc} = 0.008. The crack band width was taken as 50 mm and w_f = 0.5 mm. A single flexibility frame element was used to model the beam with 19 integration points through the section depth and 19 along the half length. The load versus mid-span displacement of the beam is shown in Fig. 12 and the results are compared with the other available numerical results (Foster 1992). The value of failure load obtained from experiment, parabolic shear and shear model-3 is 378 kN, 441 kN and 371 kN, respectively. It is observed that the shear model-3 predicts the failure load with good accuracy with the predicted failure being diagonal tension, as observed in the test. On the other hand, the ordinary parabolic shear model overestimates the failure load and predicts yielding of the main tensile reinforcement.

8.3 Cyclic analysis of a beam-column

Low and Moehle (1987) studied the behavior of a reinforced concrete cantilever beam-column subjected to a constant axial load and with a variable lateral displacement applied at its tip. The

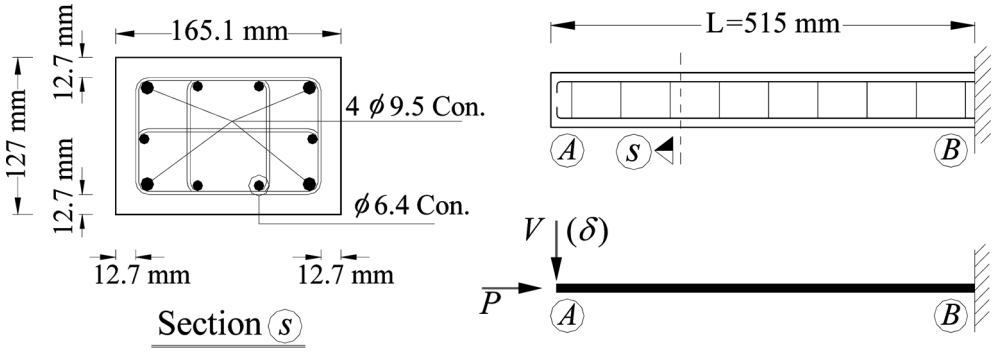

Fig. 13 Geometry and section details of the beam-column

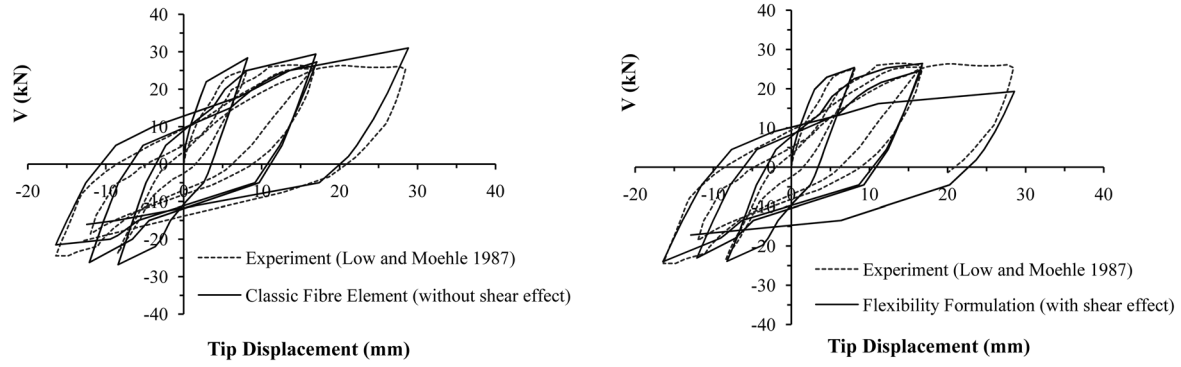

Fig. 14 Tip load-displacement of the cantilever beam-column, (a) classic fiber element without shear effect (b) present study with shear effect

geometry of the sample and cross section are shown in Fig. 13. The material properties are f_y= 450 MPa, $E_s = 2.0 \times 10^5$ MPa, f_t= 2.3 MPa, f_c = 35 MPa, E_c= 2.6×10^4 MPa, $\varepsilon_c = 0.002$, $\varepsilon_{uc} = 0.01$ and the constant axial force was $P = 44.5$ kN. The confinement effect is taken into account by adopting the Mander *et al*. (1988) model. The crack band width was taken as 15 mm and $w_f = 0.5$ mm. A single flexibility frame element was used to model the cantilever with a composite Simpson integration scheme with 9 points along the element and 15 points through the depth. The lateral load versus displacement of the free end obtained from classical flexibility element (without shear effects) and this study (including shear effects) are shown in Figs. 14(a) and 14(b), respectively. The response obtained from flexibility element with shear effect is softer at higher levels of cyclic displacement and can capture a portion of the pinching effects. A second part of the pinching effect caused by bond slip is not modeled and, therefore, not captured.

8.4 Dynamic analysis of a portal frame subjected to ground acceleration

A two-storey frame tested by Clough and Gidwani (1976) is analyzed. The geometry of the frame and details of sections and loadings are shown in Fig. 15(a). The material properties are f_y= 350 MPa, $E_s = 2.0 \times 10^5$ MPa, f_t= 2.5 MPa, f_c = 30 MPa, E_c= 2.7×10^4 MPa, $\varepsilon_c = 0.002$ and

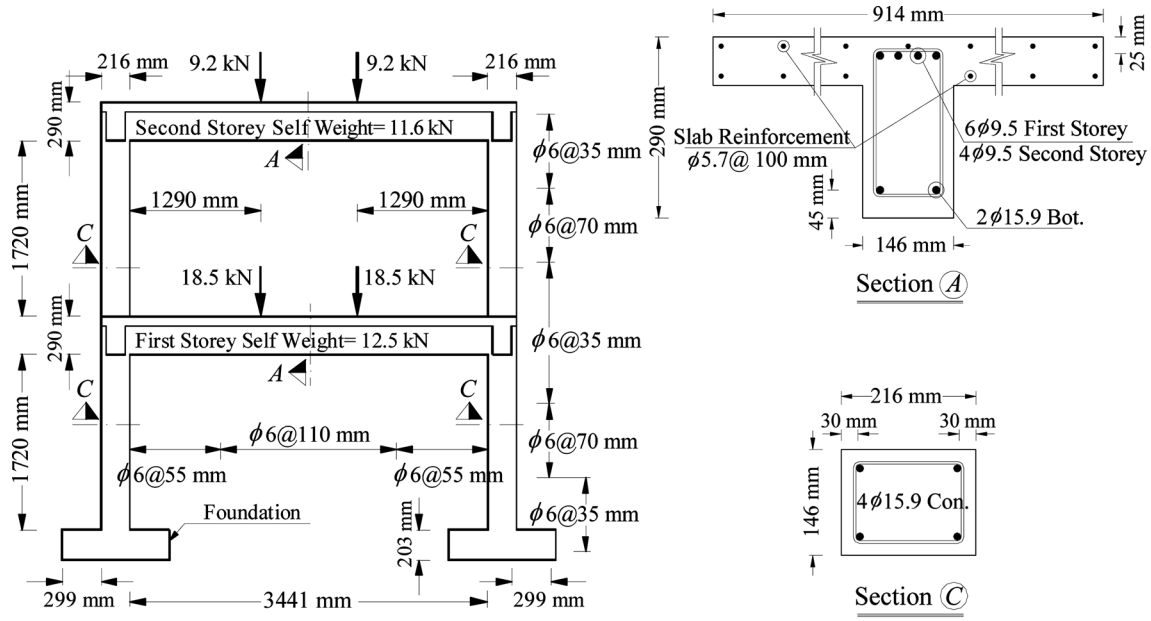

(a)

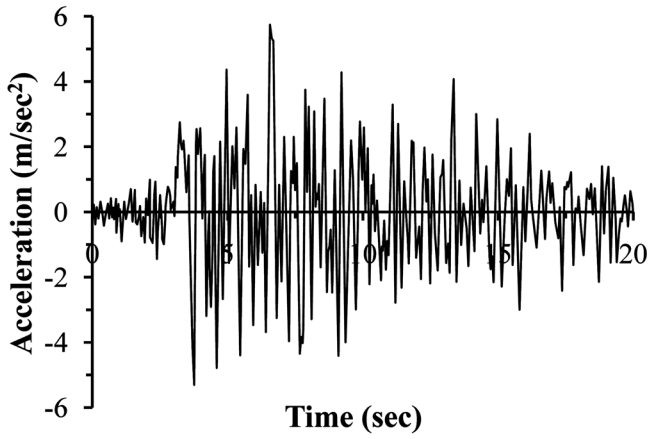

(b)

Fig. 15 (a) Geometry of frame and section details for Clough and Gidwani (1976) test, (b) N69W Taft accelerogram record scaled to 0.57g

$\varepsilon_{uc} = 0.01$. The confinement effect is taken into account by adopting the Mander *et al.* (1988) model and the crack band width was taken as 25 mm and $w_f = 0.5$ mm.

The frame was subjected to three consecutive ground acceleration histories on the shaking table. Each of these motions corresponds to the N69W Taft accelerogram recorded during the Arvin-Tahachapi earthquake of 21 July, 1952. The second test with acceleration record shown in Fig. 15(b) is studied in this example.

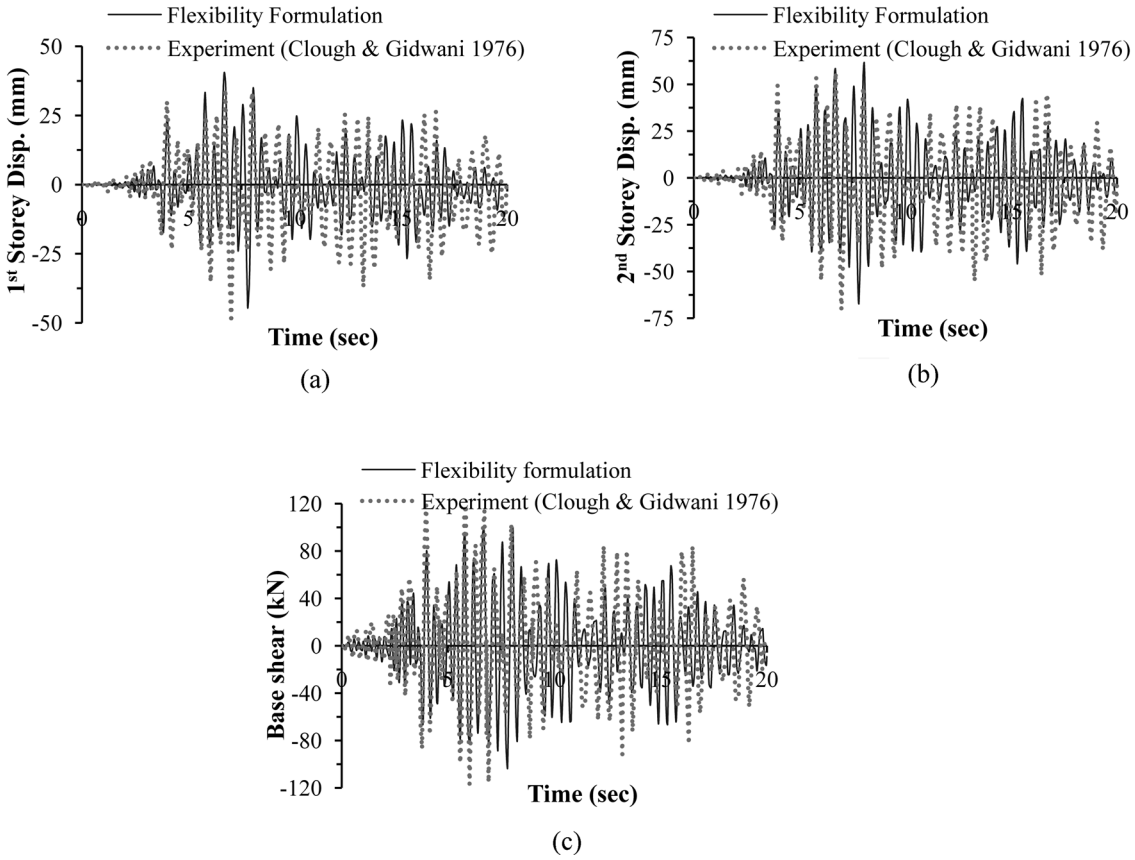

Fig. 16 (a) First storey lateral displacement, (b) second storey lateral displacement, (c) base shear versus time for Clough and Gidwani (1976) frame

Table 1 Comparison of maximum displacement and base shear obtained from experiment and flexibility formulation

	Experiment	Flexibility Formulation
1st Storey Disp.	49.8	44.6
2nd Storey Disp.	70.1	67.0
Base Shear	118.1	103.8

Using the flexibility formulation developed above, the frame was modelled with just 6 elements, one per member. A Simpson scheme with 21 integration points over the section depth and 19 and 27 integration points along the columns and beams axis, respectively, were used. A Newmark time integration scheme with a maximum time step of 0.05 sec was employed and a Rayleigh damping with $\alpha = 0.001$ (mass multiplier) and $\beta = 0.00001$ (stiffness multiplier) was adopted. The history of first and second storey lateral displacement and the base shear are shown in Fig. 16. The maximum value of lateral displacements and base shear are given in Table 1. It is seen that the analytical results correlate reasonably well with the experimental data, noting that the bond slip has been ignored in this model.

9. Conclusions

A 1D force-based reinforced concrete frame element is derived based on the total secant stiffness. The P-Δ geometrical nonlinearity effects and material nonlinearity including softening of concrete in tension and compression is taken into account by a hypo-elastic model. The effects of shear tractions at the material level are considered by employing a predefined shear flow function. Two types of function (constant and parabolic) are used for estimating shear over the section depth and it is shown that their performance is similar. A novel shear distribution is introduced in a way consistent with the adopted concrete model. It is shown that the new shear distribution has the capability to predict the ultimate shear failure load of the element with reasonable accuracy, whereas distributing the shear flow over the total depth of the section overestimates the failure load of members without transverse reinforcement. The problem of objectivity due to concrete softening is addressed and a simple technique based on the crack band concept is derived to ensure objectivity.

Finally, it is to be generally noted that the efficiency of solution, as measured by overall computational time, of force based finite element is vastly superior over that of their more widely adopted displacement based counterparts and are well suited for non-linear analysis of large scale framed structures. Historically, however, the weakness of single element force based 1D elements has been their inability to capture shear effects easily and with sufficient accuracy. In this paper a new approach has been developed that overcomes this disadvantage. The accuracy of the formulation has been demonstrated with four numerical examples where, in each case, the response has been shown to be captured well using a single 1D element.

References

Balan, T.A., Spacone, E. and Kwon, M. (2001), "3D hypoplastic model for cyclic analysis of concrete structures", *Eng. Struct.,* **23**(4), 333-342.

Bazant, Z.P. and Jirasek, M. (2002), "Nonlocal integral formulations of plasticity and damage: Survey of progress", *J. Eng. Mech.,* **128**(11), 1119-1149.

Bazant, Z.P. and Oh, B.H. (1983), "Crack band theory for fracture of concrete", *Mater. Struct.,* **16**(93), 155-177.

Bresler, B. and Scordelis, A.C. (1963), "Shear strength of reinforced concrete beams", *ACI J.,* **60**(1), 51-74.

Burns, N.H. and Siess, C.P. (1962), "Load-deformation characteristics of beam-column connections in reinforced concrete", *Report No. SRS 234*, University of Illinois, Urbana.

Carol, I. and Murcia, J. (1989), "Nonlinear time-dependent analysis of planar frames using an 'exact' formulation. I. Theory", *Comput. Struct.,* **33**(1), 79-87.

Cervenka, J., Bazant, Z.P. and Wierer, M. (2005), "Equivalent localization element for crack band approach to mesh-sensitivity in microplane model", *Int. J. Numer. Meth. Eng.,* **62**(5), 700-726.

Cervenka, V., Pukl, R., Ozbolt, J. and Eligehausen, R. (1995), "Mesh sensitivity effects in smeared finite element analysis of concrete fracture", *FRAMCOS 2*, 1387-1396.

Clough, R.W. and Gidwani, J. (1976), "Reinforced concrete frame 2: Testing and analytical correlation", *Report No. EERC 76/15*, Earthquake Engineering Research Centre, University of California, Berkeley.

Crisfield, M.A. and Wills, J (1989), "Analysis of R/C panels using different concrete models", *J. Eng. Mech.,* **115**(3), 578-597.

Darwin, D. and Pecknold, D.A.W. (1974), "Inelastic model for cyclic biaxial loading of reinforced concrete", *Civil Engineering Studies, Structural Research Series (University of Illinois at Urbana-Champaign, Department of Civil Engineering),* No. 409, P.169.

De Borst, R. (2003), "Numerical aspects of cohesive-zone models", *Eng. Fract. Mech.,* **70**(14), 1743-1757.

Foster, S.J. (1992), "The structural behaviour of reinforced concrete deep beams", PhD Dissertation, University

of NewSouth Wales, Australia.
He, W., Wu, Y.F., Liew, K.M. and Wu, Z. (2006), "A 2D total strain based constitutive model for predicting the behaviors of concrete structures", *Int. J. Eng. Sci.,* **44**(18-19), 1280-1303.
Kupfer, H., Hilsdorf, H.K. and Rusch, H. (1969), "Behaviour of concrete under biaxial stress", *ACI J.,* **66**(8), 656-666.
Low, S.S. and Moehle, J.P. (1987), "Experimental study of reinforced concrete columns subjected to multi-axial cyclic loading", *Report No. EERC 87/14*, Earthquake Engineering Research Centre, University of California, Berkeley.
Mander, J.B., Priestley, M.J.N. and Park, R. (1988), "Theoretical stress-strain model for confined concrete", *J. Struct. Eng.,* **114**(8), 1804-1826.
Markeset, G. and Hillerborg, A. (1995), "Softening of concrete in compression-localization and size effects", *Cement Concrete Res.,* **25**(4), 702-708.
Neuenhofer, A. and Filippou, F.C. (1997), "Evaluation of nonlinear frame finite-element models", *J. Struct. Eng.,* **123**(7), 958-966.
Neuenhofer, A. and Filippou, F.C. (1998), "Geometrically nonlinear flexibility-based frame finite element", *J. Struct. Eng.,* **124**(6), 704-711.
Park, J.W. and Kim, S.E. (2008), "Nonlinear inelastic analysis of steel-concrete composite beam-columns using the stability functions", *Struct. Eng. Mech.,* **30**(6), 763-785.
Petrangeli, M., Pinto, P.E. and Ciampi, V. (1999), "Fibre element for cyclic bending and shear of RC structures. I: theory", *J. Eng. Mech.,* **125**(9), 994-1001.
Sezen, H. (2008), "Shear deformation model for reinforced concrete columns", *Struct. Eng. Mech.,* **28**(1), 39-52.
Shuraim, A.B. (2001), "Variable layering system for nonlinear analysis of reinforced concrete plane frames", *Struct. Eng. Mech.,* **11**(1), 17-34.
Taylor, R.L., Filippou, F.C., Saritas, A. and Auricchio, F. (2003), "A mixed finite element method for beam and frame problems", *Comput. Mech.,* **31**(1-2), 192-203.
Valipour, H.R. and Foster, S.J. (2010), "A Total secant flexibility-based formulation for frame elements with physical and geometrical nonlinearities", *Finite Elem. Anal. Des.,* **46**(3), 288-297.
Vecchio, F.J. and Collins, M.P. (1988), "Predicting the response of reinforced concrete beams subjected to shear using modified compression field theory", *ACI Struct. J.,* **85**(3), 258-268.
Yun, G.J., Harmon, T.G., Dyke, S.J. and So, M. (2008), "A total strain-based hysteretic material model for reinforced concrete structures: Theory and verifications", *Comput. Concrete,* **5**(3), 217-241.

Appendix

The secant stiffness matrix in the local coordinate system for the *i*th iteration is

$$ {}^{i}\mathbf{C}_{\text{sec}} = \begin{bmatrix} c_{11} & c_{12} & c_{13} \\ & c_{22} & c_{23} \\ sym. & & c_{33} \end{bmatrix} \tag{A1} $$

where c_{ij} are material stiffness components in the *x-y* global coordinate system and are obtained from the Eq. (26). For computational efficiency, the coefficient terms of Eq. (A1) are pre multiplied to give

$$ c_{11} = G^{*} \sin^2 2\alpha + \frac{1}{1-\upsilon^2}\left\{\upsilon\sqrt{E_1 E_2}\,\frac{\sin^2 2\alpha}{2} + (E_1 + E_2)\cos^4\alpha - E_2 \cos 2\alpha\right\} \tag{A2} $$

$$ c_{12} = c_{12} = -G^{*} \sin^2 2\alpha + \frac{1}{1-\upsilon^2}\left\{\upsilon\sqrt{E_1 E_2}\left(1 - \frac{\sin^2 2\alpha}{2}\right) + (E_1 + E_2)\,\frac{\sin^2 2\alpha}{4}\right\} \tag{A3} $$

$$ c_{13} = c_{31} = -G^{*}\,\frac{\sin 4\alpha}{2} - \frac{\sin 2\alpha}{2\,(1-\upsilon^2)}\{\upsilon\sqrt{E_1 E_2}\cos 2\alpha + E_2\,\sin^2\alpha - E_1\,\cos^2\alpha\} \tag{A4} $$

$$ c_{22} = G^{*} \sin^2 2\alpha + \frac{1}{1-\upsilon^2}\left\{\upsilon\sqrt{E_1 E_2}\,\frac{\sin^2 2\alpha}{2} + (E_1 + E_2)\cos^4\alpha - E_1 \cos 2\alpha\right\} \tag{A5} $$

$$ c_{23} = c_{32} = G^{*}\,\frac{\sin 4\alpha}{2} + \frac{\sin 2\alpha}{2\,(1-\upsilon^2)}\{\upsilon\sqrt{E_1 E_2}\cos 2\alpha + E_1\,\sin^2\alpha - E_2\,\cos^2\alpha\} \tag{A6} $$

$$ c_{33} = G^{*} \cos^2 2\alpha - \frac{1}{1-\upsilon^2}\left\{\upsilon\sqrt{E_1 E_2}\,\frac{\sin^2 2\alpha}{2} - (E_1 + E_2)\frac{\sin^2 2\alpha}{4}\right\} \tag{A7} $$

where, α is the current orientation of the principal stress (strain) coordinate system with respect to *x-y* global coordinate system. In the first iteration an initial guess of $\alpha = 0$, $E_1 = E_2 = E_c$ and $\upsilon = \upsilon_0$ can be used.